Visual Analysis of Two-Phase Flow Displacement Processes in Porous Media

S. Frey[1,2] , S. Scheller[2], N. Karadimitriou[2] , D. Lee[2] , G. Reina[2] , H. Steeb[2] and T. Ertl[2]

[1]University of Groningen, Netherlands
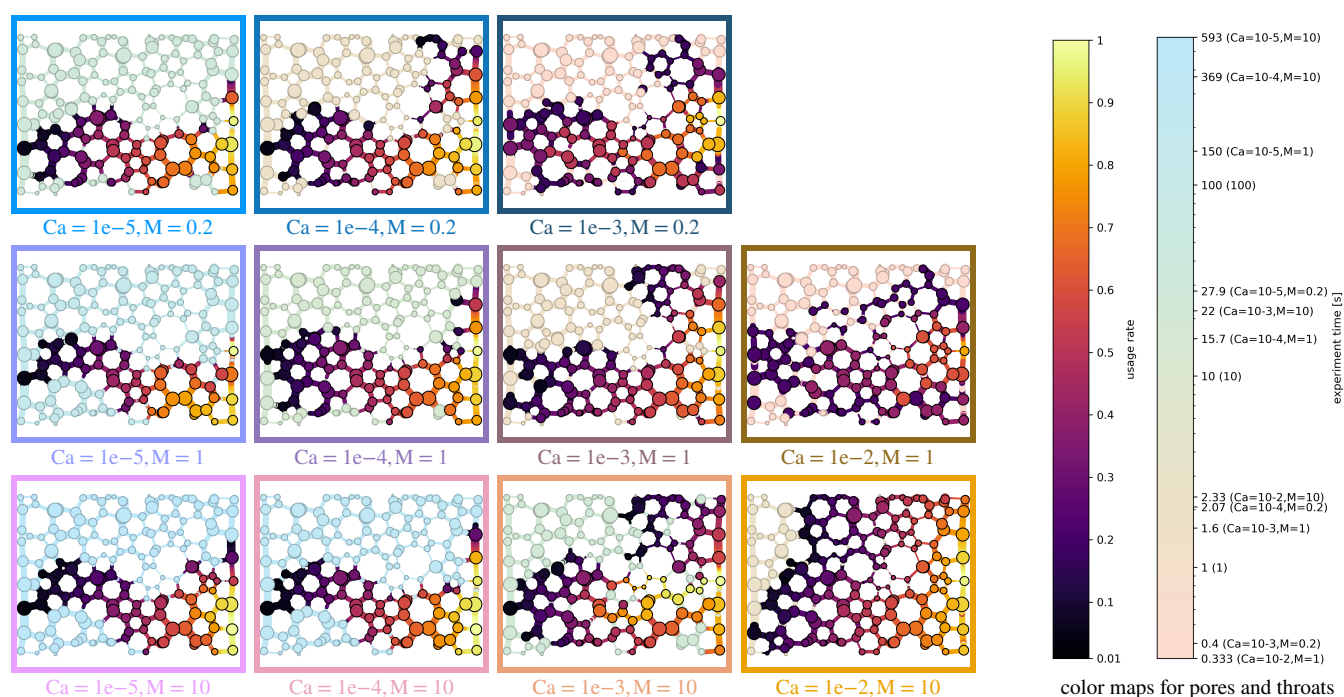[2]University of Stuttgart, Germany

Figure 1: Transport networks visualize paths in the porous medium occupied by one fluid phase (non-wetting) injected from the right when displacing another fluid (wetting), depicted until breakthrough (i.e., the non-wetting phase establishes an uninterrupted connection from right to left). The matrix layout reflects the position in parameter space with respect to capillary numbers Ca and viscosity ratios M. Corresponding glyphs (■) representing each configuration by a colored cell are used for efficient communication. In experiments with low Ca (■) the non-wetting fluid evolves in a narrow path from right to left, an effect commonly referred to as "capillary fingering", indicating the dominance of capillary forces. Decreasing M (■) in the experiments yields a broader path, and further increasing Ca (■) introduces new flow paths in the upper part which evolve much later than the main flow (so-called "viscous fingering"). High Ca and M (■) yield an almost uniform ("piston-like") progression of the flow from right to left, hinting at predominant viscous forces.

Abstract

We developed a new visualization approach to gain a better understanding of the displacement of one fluid phase by another in porous media. This is based on a recent experimental parameter study with varying capillary numbers and viscosity ratios. We analyze the temporal evolution of characteristic values in this two-phase flow scenario and discuss how to directly compare experiments across different temporal scales. To enable spatio-temporal analysis, we introduce a new abstract visual representation showing which paths through the porous medium were occupied and for how long. These transport networks allow to assess the impact of different acting forces and they are designed to yield expressive comparability and linking to the experimental parameter space both supported by additional visual cues. This joint work of porous media experts and visualization researchers yields new insights regarding two-phase flow on the microscale, and our visualization approach contributes towards the overarching goal of the domain scientists to characterize porous media flow based on capillary numbers and viscosity ratios.

CCS Concepts

• *Human-centered computing* → *Visualization;* • *Applied computing* → *Environmental sciences;*

1. Introduction

A porous medium is a material containing interconnected void spaces. Understanding fluid flow through such a medium is at the core of porous media research. Two-phase flows and specifically their displacement processes are highly relevant for various industrial and environmental applications, including enhanced oil recovery [AMW*17], soil remediation [FHR04], printing [KLG10], etc. However, the underlying physical processes are not fully understood yet and are subject of experimental investigations and simulations.

In this work, we discuss our visual analysis approach to study the forced displacement of a fluid saturating the void space by another fluid that is injected into the porous medium in a laboratory setting. Depending on the parameters of the conducted experiments, the liquids behave differently, and the time required for the injected fluid to traverse the medium also varies strongly. To derive insights from the captured fluid progression, we propose to extract several metrics that characterize each experiment. To enable the analysis of the spatio-temporal changes in the distribution of the fluids, we extract pore networks. They allow to both capture the spatial progress of the injected fluid as well as establishing a correlation between the pore geometry and the behaviour of the fluid. With our method, we are able to classify the conducted experiments into groups of similar behaviour. We discuss how the previously established dependency on specific experimental parameters is misconceived and that prior metrics do not properly reflect the local behaviour of a porous medium. In the remainder of this section we introduce necessary background on porous media fundamentals, before outlining our analysis goals in this paper.

1.1. Fundamentals of Porous Media

A porous medium contains solid material and a distribution of void space. Porosity denotes the ratio of the void volume over the bulk volume of the porous medium. The void spaces can be categorized into *pores* (large void space) and *throats* (narrow spaces connecting the bodies), see Fig. 2. Pore bodies and pore throats are generally interconnected so that flow through the porous medium can occur.

In this work, we study the forced displacement of a wetting fluid by an incoming non-wetting fluid in a porous medium. This process is referred to as drainage (the term imbibition denotes the opposite). In an experimental setup, the formation of an uninterrupted connection of displacing fluid between its entry into the system on one side and its exit on another side is a key event commonly denoted as breakthrough. The concept of wettability and the corresponding differentiation of the fluids into wetting and non-wetting phases expresses the affinity of a fluid towards the solid surface as a result of intermolecular interactions at the *fluid-solid interface*: the wetting fluid has an increased affinity—i.e., stronger adhesive forces—towards the solid, while the opposite holds for the non-wetting fluid.

Two types of forces are the most relevant when studying displacement processes in a porous medium. *Capillary forces* cause slow fluid displacement dictated exclusively by the geometry of the pore space (*pores* and *throats*). With imbibition, capillarity can drive flow in narrow spaces even against forces like gravity (e.g., paper absorbing water). This *capillary flow* is driven by tension at the *fluid-fluid interface* and the wetting properties regarding the solid phase at the
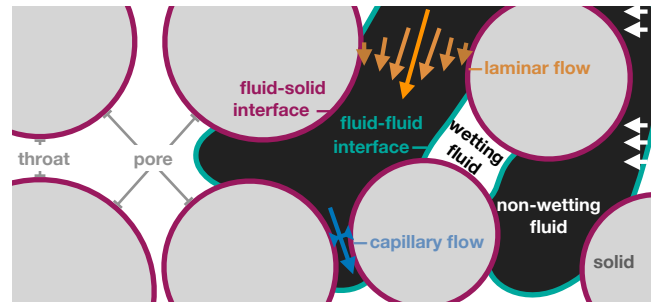

Figure 2: *Illustration of basic terminology in a focused domain of the porous medium under investigation (with a porosity of 0.5).*

fluid-solid interface. *Viscous forces* are induced by friction between fluid and solid walls which slows down the flow at the boundary of a fluid, generating layers of different velocities. These, in turn, induce shear stresses acting in parallel to these layers, propagating the slowing effect from solid walls to inner fluid layers. Hence, this yields *laminar flow* in which a fluid flows in internal layers of different velocities along its cross-section. The internal friction between a fluid's layers and the impact on its flow is expressed via viscosity. This is proportional to the velocity gradient between layers, and for high velocities the flow is called "viscosity driven".

Two numbers are commonly used to characterize flow. The *capillary number* Ca is a dimensionless quantity representing the relative effect of viscous forces versus capillary forces. It is commonly expressed as the product of viscosity and fluid velocity, divided by interfacial tension. As a rule of thumb, for low capillary numbers ($\lesssim 1e-5$) flow in porous media is dominated by capillary forces, whereas for high capillary numbers ($\gtrsim 1e-3$) the capillary forces are negligible compared to viscous forces; a combination of both forces is in effect for for intermediate capillary numbers. The *viscosity ratio* M depicts the relation between the viscosity of the invading fluid—the non-wetting phase for the drainage scenario in this work—to this of the defending fluid—the wetting phase.

1.2. Analysis Goals

The overarching goal of this work is to characterize flow based on the capillary number Ca and viscosity ratio M. A series of experiments yields 2D+time grayscale image data for different combinations of Ca and M (Sec. 3.1), from which we extract three phases: the non-wetting and wetting fluids, and the solid phase (Sec. 3.2). We then address three analysis questions, which in combination support our overarching goal. To begin with, we study *how the temporal evolution of relevant output quantities, like saturation, disconnected components, and interfacial area is governed by Ca and M (Q1)*. These scalar quantities indicate quantitatively how Ca and M affect the displacement process at a given time. The geometry of the porous medium also has a crucial impact on the acting forces. In narrow areas capillary forces are generally more relevant, while in larger pore spaces the impact of viscous forces is higher. Regarding the spatial evolution of the flow, we then analyze *how the spatial displacement patterns change (Q2)*, and *how pore throat widths influence local flow properties (Q3)*. Our visualization approach supporting these analysis tasks is described in-depth in Sec. 4 ff.

2. Related Work in Visualization and Porous Media Research

Visualization of porous media and liquid phases. Earlier work focused mostly on the rendering of porous media: Grottel et al. [GRZ*10] show different approaches employing geometry shaders, or ray casting, while Naumov et al. [NBK13] investigate rendering flow in a porous medium in a virtual reality environment and tackling occlusion issues. Zhang et al. [ZFS*18] extracted CO_2 bubbles and their surrounding geometry in a liquid-filled sandstone sample from X-ray computed tomography data. They automatically classify and correlate bubbles with similar interface morphology and geometric features and support the search for pore geometries that favor the sequestration of CO_2 bubbles. De Winter et al. [dWWS*20] investigate the behavior of single-phase flow in microfluidics from experimental recordings via confocal microscopy. Among others, they visualize the boundaries between different flow regions and depict transport mechanisms via streamlines and animated renderings. The Scientific Visualization Contest 2016 featured a particle simulation ensemble of salt dissolving in water, developing viscous fingers [GG16]. This data set was the focus of several approaches, also beyond the contest scope. Gralka et al. [GGS*18] describe a system for the visual and structural investigation of this data via multiple views, drilling down from diagrams of ensemble metrics to investigation of the 3D data, abstracted finger topology and vortex core lines forming in the data. Favelier et al. [FGT16] extract and track the emerging fingers based on topological data analysis and visualize their properties in comparative line plots. Lukasczyk et al. [LAS*17] extended this, incorporating tracking graphs ([WCBP12]) to investigate a single simulation and a query interface coupled to thumbnails of a Paraview Cinema database to investigate the ensemble as a whole. An alternative approach complements the 3D and structure views by glyphs summarizing high-level parameters of single members of the ensemble [LBS*18]. Soler et al. [SPD*19] rank an ensemble of viscous fingering simulations according to their agreement with a ground-truth data set. To this end they propose a novel metric that combines geometric and topological features based on persistence diagrams. Xu et al. [XDH*19] use Reeb graphs to extract viscous and gravitational finger structures and the respective skeletons, which are abstracted into glyphs and tracked over time. They also demonstrate a tracking graph augmented with the glyphs as well as an analysis system which allows for interactively browsing through the spatial domain as well as the extracted fingers.

Ensemble visualization. The analysis of ensemble data generally is a challenging visualization task [OJ14]. Kehrer et al. [KH13], Sedlmair et al. [SHB*14], and Wang et al. [WHLS19] provided detailed surveys of related techniques. Potter et al. [PWB*09] as well as Sanyal et al. [SZD*10] proposed early approaches to study climate ensembles, while Waser et al. [WFR*10] described a system for the interactive steering of simulation ensembles. Bruckner and Möller [BM10] employ squared differences to explore a simulation space, Hummel et al. [HOGJ13] compute region similarity via joint variance, and Kumpf et al. [KRRW19] track statistically-coherent regions using optical flow. Hao et al. [HHB16] calculate shape similarities for particle data using an octree structure, while He et al. [HGSP20] employ surface density estimates for distances between surfaces.

Porous Media Research. Macroscale models for two-phase flow in porous media have been proposed and widely applied. Van Genuchten [VG80] introduced a model putting the capillary pressure arising from capillary forces in a simplified, non-linear relation to the wetting phase saturation. Based on thermodynamic principles and approaches, it has been shown that capillary pressure crucially also depends on its spatial distribution in the porous domain [SBR*16]. Theories which accordingly include more state variables than saturation are denoted as extended theories. Hassanizadeh and Gray [HG93] proposed to use interfacial area between phases as a separate state variable in addition to saturation. Extended theories can also include process variables dependent on higher-order morphological features [KS14] which can be expressed with the first three Minkowski functionals *M0 –M2* [Web01].

Two-phase flow has been studied in experiments with natural or artificial porous media. Mostly rock samples are used as natural porous media [BRB*16, BOK*13, ABB13], and many approaches exist to manufacture artificial porous media with well-defined properties [Dar57, GCS88, Sha98, CCR97]. Karadimitriou and Hassanizadeh [KH12] introduced the term micromodel to describe an artificial, transparent porous medium with similar average properties—like pore size distribution and porosity—to a natural porous medium on the centimeter scale. Micromodels are commonly produced either by etching processes [MK61], or lithography [Tho83]. Soft-lithography specifically is widely employed due to its comparably low cost and high precision [XW98]. We also use it in this work to create a micromodel from Poly-Di-Methyl-Siloxane (PDMS).

Lenormand et al. [LTZ88] numerically and experimentally investigated the impact of capillary numbers Ca and viscosity ratios M via qualititative observations. They categorized the flow regimes into *capillary fingering* for low Ca, *viscous fingering* for increased Ca and low M, as well as *stable front* for elevated Ca and M. Cheng et al. [CPNNG04] performed drainage and imbibition experiments to investigate the role of the interfacial area between fluids as a separate state variable under quasi-static flow conditions. Karadimitriou et al. [KHJNK14] discuss this under dynamic conditions (using a PDMS micromodel), concluding that interfacial area can only be used under quasi-static but not under dynamic conditions. They attributed this mostly to phases getting disconnected, but could not quantify and further analyze this in detail as we do now.

3. Experiments and Image Analysis

We conducted experiments to study the distribution of the two fluid phases depending on capillary numbers Ca and viscosity ratios M for a fixed pore geometry (Sec. 3.1). The three involved phases—solid, wetting fluid, and non-wetting fluid—are then extracted from the resulting time-dependent ensemble for further analysis (Sec. 3.2).

3.1. Experiments

All experiments use an artificial porous medium made of Poly-Di-Methyl-Siloxane (PDMS) via soft lithography [XW98, KMK*13] (replicating the so-called C-type network from Sivanesapillai and Steeb [SS18]). The pore geometry was generated by positioning cylindrical pillars of various diameters at various locations, yielding a mean pore size of 410 μm and a porosity of 0.44.
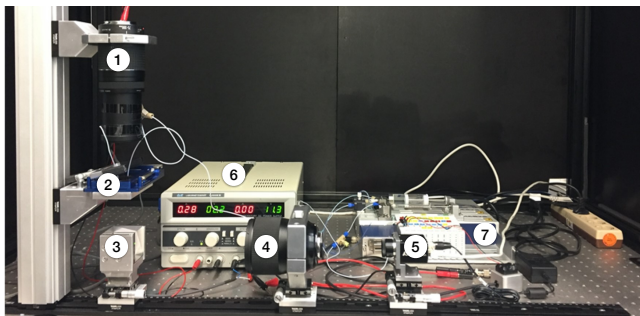
Figure 3: Optical setup capturing the experiments: (1) LED source mounted to an objective lens, (2) the stage for the micro-model, (3) a prism, (4) a telephoto lens, (5) an industrial camera (connected to a PC via Ethernet), (6) a stable power supply, and (7) the syringe pumps. The setup was placed on a vibration-free optical table.

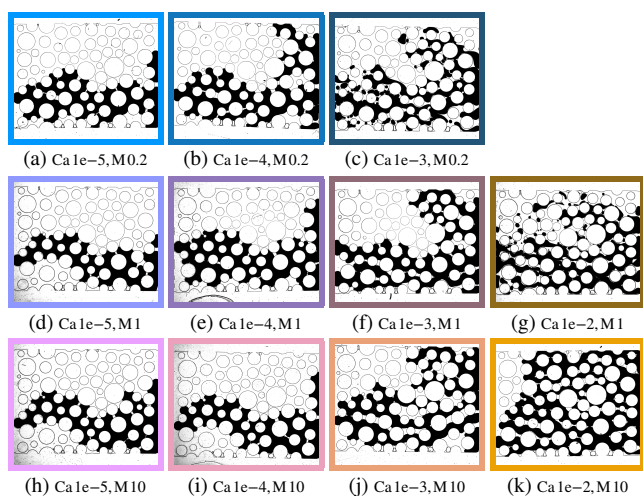| (a) Ca 1e−5, M 0.2 | (b) Ca 1e−4, M 0.2 | (c) Ca 1e−3, M 0.2 | |
| (d) Ca 1e−5, M 1 | (e) Ca 1e−4, M 1 | (f) Ca 1e−3, M 1 | (g) Ca 1e−2, M 1 |
| (h) Ca 1e−5, M 10 | (i) Ca 1e−4, M 10 | (j) Ca 1e−3, M 10 | (k) Ca 1e−2, M 10 |

Figure 4: Experiment recordings at breakthrough (an uninterrupted connection exists between left and right boundary, Sec. 5.2).

The resulting distribution of sizes for the corresponding pore bodies and throats creates a certain degree of local pore space heterogeneity. It allows to observe local and global flow differences even though the porous medium is not varied across experiments (incorporating other geometries in our experiments remains for future work).

We consider a drainage scenario: the pore space is entirely saturated with the wetting phase initially. It is then displaced by the non-wetting phase streaming into the system from the so-called inlet on the right side and leaving at the outlet on the left. Fluorinert FC-43 serves as the wetting phase that is displaced by water dyed with ink, as the non-wetting phase. Water itself yields a viscosity ratio $M = 0.2$. With the addition of glycerol also $M = 1$ and $M = 10$ were realized. The flux at which the fluid is introduced into the porous medium from the right is accordingly adjusted to achieve capillary numbers of $Ca \in \{1e−5, 1e−4, 1e−3, 1e−2\}$. Due to technical challenges and induced deformation of the micromodel, the combination of $Ca = 1e−2$ and $M = 0.2$ was excluded from the data.

PDMS is naturally transparent which allows using transmitted light microscopy (Fig. 3) to capture flow at a resolution of 8 microns/pixel at 1–15 fps (depending on the speed of the investi-

| (a) original capture | (b) manual cleaning | (c) post-processing |

Figure 5: Mask pre-processing phases (zoom-in, Ca 1e−5, M 1).

gated process). This yields a gray-scale 8-bit image sequence with a resolution of 2448×2050 pixels per image for every experiment (e.g., Fig. 4). The wetting phase, PDMS, and some trapped air appear as light-gray to white pixels, while the non-wetting fluid, interfaces and dust particles appear as dark-gray to black pixels (Fig. 5a). The porous media model is flushed and heated between experiments to remove residual fluids. This leads to translational and rotational displacements, as well as slight perspective changes. To compensate for this, we capture one mask image before the non-wetting fluid enters and align captured images accordingly (see *Enhanced Correlation Coefficient (ECC)* [EP08]), using (Ca 1e−2, M 1) as reference. The mask is further used to distinguish between pore space and solid.

3.2. Phase Segmentation

In the recorded masks, the walls of the Poly-Di-Methyl-Siloxane (PDMS) geometry appear as ≈ 10 pixel wide contours with a dark-gray to black tone that becomes lighter towards the edge (see closeup in Fig. 5a). The contours exhibit noise in brightness and thickness due to material and lighting imperfections. Dust particles from the air deposit on the model and appear as stains with arbitrary gray values. Furthermore, the model geometry features dead-end pores at the top and bottom which trap air bubbles that cannot be flushed out and make the space inaccessible to the fluids. These air bubbles appear as translucent material with a dark-gray to black contour.

Mask images are cleaned manually (removing trapped air bubbles, Fig. 5b), denoised with a 5×5 median blur filter, and binarized (pixel values < 128 yield black, white otherwise). Remaining artifacts below the minimum pore throat size are further reduced by applying three iterations of morphological opening and closing operations with a 3×3 kernel (e.g., [HSZ87]). Finally, tiny connected regions with contours of < 150 pixels are removed to account for smaller artifacts (e.g., due to dust particles) [S*85] (Fig. 5c). This conservatively yields a limited number of remaining artifacts, but crucially small fluid components and fine pore geometry remain intact. The images captured during the experiment are pre-processed just like the masks, but without initial manual editing. The non-wetting phase corresponds to all black pixels, assigning the remaining pixels to the wetting phase (Fig. 6c).

4. Visual Analysis Approach

We now outline analysis questions regarding porous media research and motivate the design of our visualization approach. In the analysis, our first step is to understand *(Q1) how descriptive quantities are governed by Ca and M*. The three considered quantities—saturation, disconnected components, and interfacial area—capture important characteristics of the displacement process for each time step of
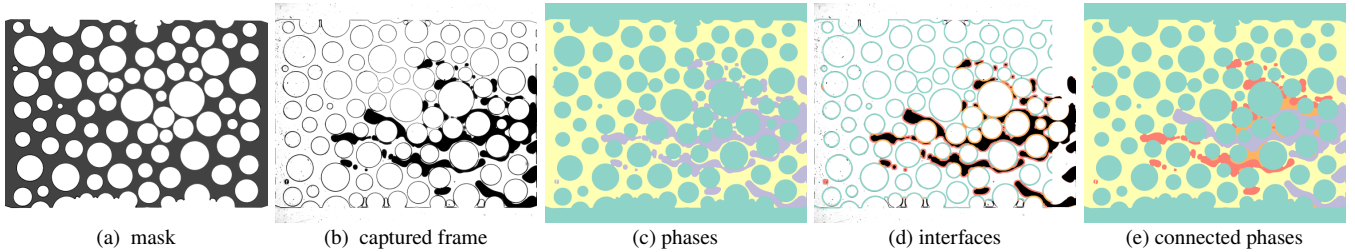
(a) mask   (b) captured frame   (c) phases   (d) interfaces   (e) connected phases

Figure 6: *Phase segmentation and interface extraction example for (Ca = 1e−2, M = 1). (a) Using the mask, (b) captured images are (c) segmented into solid, wetting and non-wetting phase (Sec. 3.2). (d) We further compute interfaces between all phase combinations. (e) The fluid phases are further partitioned into parts with and without uninterrupted connection to (i) the inlet on the right for the non-wetting phase (disconnected parts depicted in red), and (ii) the outlet on the left for the wetting phase (disconnected parts shown in orange).*
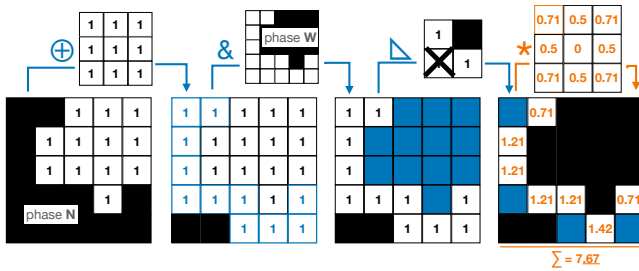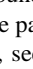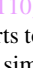

Figure 7: *Five steps determining the interface length between phases* **N** *and* **W** *from left to right (bitwise operations:* blue; *floating point operations:* orange*). Changes to the previous state are indicated in the respective color. White pixels of* **N** *are expanded via dilation (*⊕*), before the bitwise AND of* **N** *and* **W** *yields their interface (&). Corner pixels are removed from the interface (⌐), and distances of pixel to their neighbors are computed via convolution (∗). Finally, the interface length is the sum of pixel distances (∑).*

each experiment (Sec. 5.1 and Fig. 7). This multivariate visualization problem is addressed on the basis of line charts which are well accepted and easily understood in the application domain. All experiments are shown in each chart for direct comparability (Fig. 8, discussion in Sec. 6). Variations in Ca and M yield differences of about three orders of magnitude in the duration of displacement processes (between 330 ms and 593 s). In one case (Fig. 8a) we address this with a logarithmic scale of physical time. In Fig. 8b and Fig. 8c as well as in further visualizations throughout this work we instead employ temporal normalization based on breakthrough—an event which is fundamentally important for the analysis (Sec. 5.2).

Linking lines in the chart to their corresponding position in parameter space is crucial for the analysis. To support this, we use a bivariate color map with dimensions Ca and M. We further introduce dedicated glyphs designed to intuitively represent parameter space positions for groups of experiments. The glyphs also employ the bivariate color scheme for depicting selected experiments, while conveying the full parameter space with a light gray background for context (the "missing" square in the top-right indicates the parameter combination (Ca 1e−2, M 0.2) without stable results, see Sec. 3). For instance, the group of experiments with parameter combinations {(Ca 1e−4, M 0.2), (Ca 1e−3, M 1), (Ca 1e−2, M 10)} is represented via ▪, and ▪ depicts {(Ca 1e−5, M 1), (Ca 1e−5, M 10), (Ca 1e−4, M 10)}. These glyphs are used as overlays in our charts to convey the parameter space positions of groups of lines with sim-

ilar progression, but also inline in the text to provide an intuitive parameter space link for supporting the discussion.

Under variation of Ca and M, we further aim to analyze *(Q2) how the spatial displacement pattern changes*, and *(Q3) how pore throat widths influence local flow properties*. Our line charts are only able to convey temporal aspects but not explicitly spatial progression and the impact of pore geometry. Therefore, we introduce our approach for transport networks in porous media to address *Q2* and *Q3*. A transport network is a graph with nodes corresponding to pores and edges reflecting pore throats. We associate their components with the local pore geometry (the free space not occupied by the solid, see Sec. 7.1). This allows to track the displacement progression based on spatial coverage, and relate this to said pore geometry. We employ a node-link representation of transport networks for its natural geometrical embedding in the physical setup. It provides a static (global) overview of displacement progress for individual experiments before or after breakthrough. Comparing transport network representations in a matrix layout enables the correlation between system states and parameter configurations (Sec. 7.2, see Fig. 1, Fig. 10). The layout directly represents our 2D parameter space with Ca and M—akin to the glyphs introduced above—and juxtaposition is well-suited for comparing the experiments present in our experimental ensemble.

Transport networks further allow linking flow displacement to pore space characteristics, enabling the quantitative visual analysis via transport histograms. These relate the width of pore throats to their occupancy with non-wetting fluid (Sec. 7.3, Fig. 11). Like line charts, histograms are well-understood in the domain. Via stacked bars, one combined representation can convey occupancy before and after breakthrough, as well as throats that never get saturated.

5. Visualization Data for Comparative Analysis

Interfacial length, (dis-)connected fluid components, and saturation are our quantities of interest extracted from each captured experimental image (Sec. 5.1). Direct comparison between experiments requires dealing with different temporal scales, and for this we discuss three different means of temporal normalization (Sec. 5.2).

5.1. Quantities of Interest

Interface Length. The length of the interface between the wetting and the non-wetting phase gives an indication of how significant the impact of the different forces is. We compute the interfacial length
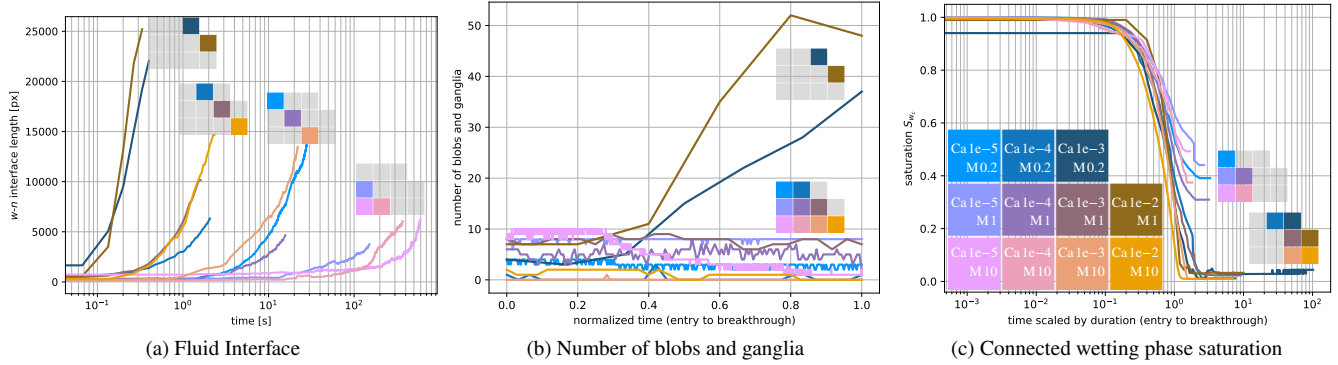
(a) Fluid Interface   (b) Number of blobs and ganglia   (c) Connected wetting phase saturation

Figure 8: *Temporal evolution of different quantities of interest across experiments. A bivariate map assigns color to each experiment regarding its corresponding Ca and M (cf. lower left quadrant in* c)*, and overlays were added to emphasize the location of identified groups of similar behavior in the parameter space (this was done manually, an automated approach is subject to future work).*

between the non-wetting phase **N** and the wetting phase **W** based on the masks from the segmentation in five steps (see Fig. 7).

⊕ We first expand white pixels in **N** by dilating with a 3×3 kernel.

& Then, we perform a bitwise AND with mask **W**. This results in one-pixel-thin lines at the interface between **N** and **W**.

◣ Filter operations then set those white pixels to black that have a white neighbor both horizontally and vertically.

∗ The sum of Euclidean distances to its neighbors is computed for each center of a (white) pixel by convolving with a 3×3 kernel. Its entries depict distances between centers—divided by two as one segment is accounted for by both corresponding pixels.

∑ Finally, the sum of pixel distances yields the total interface length.

Fluid Parts (Dis-)Connected to Inlet/Outlet. The non-wetting fluid can be disconnected from the inlet due to significant stresses induced by competing viscous forces and interfacial tension. The number of disconnected components provides complementary insight on the interplay of these forces. We check what portion of the non-wetting fluid is connected to the inlet on the right, and respectively what part of the wetting fluid is connected to the outlet on the left (Fig. 6e). For this, we consider the distance of fluid parts to the respective image border—i.e., on the left for the wetting fluid, and the right for the non-wetting fluid. For the images captured with our experimental setup, we identified a distance of 40 pixels to the border—i.e. 1.5% of the 2448 pixel wide frame—to yield reliable detection of both fluid phases across all images.

(Connected) Saturation of Fluid Phases. Saturation depicts the ratio of the pore space occupied by wetting fluid and yields insights regarding the speed of progression and eventually achieved coverage. We consider only the part of the wetting phase connected to the outlet, i.e., neglecting parts enclosed by the non-wetting fluid (so-called extended theories in the domain likewise only cover connected phases, see Sec. 2). Strictly speaking, the input images are two-dimensional projections of three-dimensional processes. However, the loss of depth information in the processes is negligible: the considered porous medium is orders of magnitude smaller in depth than in width and height, at 100 µm in comparison to 20 mm × 15 mm. Accordingly, we approximate the saturation of the fluid phases by the relative fraction of pixels per phase over the pixels belonging to the total pore space.

5.2. Temporal Normalization via Breakthrough

We need to achieve meaningful comparability of the evolution of our experiments despite their run times ranging across different orders of magnitude. For this, we use the breakthrough event—i.e., the formation of an uninterrupted connection of the non-wetting phase from the inlet on the right to outlet on the left—as a temporal reference point to normalize time individually per experiment. The behavior of the fluid before and after breakthrough is of particular interest in the analysis. For instance, depending on the experimental parameters, certain characteristics—like the continuation of saturation change—are not expected to happen after breakthrough. We obtain normalized time $\hat{t}$ from physical time t by putting it into the context of the time span from the start of the experiment t_i until breakthrough at t_b: $\hat{t} = \frac{t - t_i}{t_b - t_i}$.

6. Temporal Evolution of Characteristic Values

Visualization data and temporal normalization enable a quantitative comparison across experiments (Fig. 8). Below, line charts depict the progression of a quantity of interest across all experiments, linking lines to Ca and M via a bivariate color map and dedicated glyphs indicating position in the parameter space.

Interface between wetting and non-wetting phase (Fig. 8a)

From the visualization, we identify groups of two to three curves for which the interface length starts increasing at similar points in time:

(▦) {(Ca 1e−3, M 0.2), (Ca 1e−2, M 1)},

(▦) {(Ca 1e−4, M 0.2), (Ca 1e−3, M 1), (Ca 1e−2, M 10)},

(▦) {(Ca 1e−5, M 0.2), (Ca 1e−4, M 1), (Ca 1e−3, M 10)},

(▦) and {(Ca 1e−5, M 1), (Ca 1e−5, M 10), (Ca 1e−4, M 10)}.

Interestingly, similar behavior in this regard can be observed along "diagonals" of step-wise increases of Ca and M in the parameter space. At the boundary of our parameter space, for the transition from diagonal ▦ to ▦, it is indicated that the behavior does not change fundamentally anymore when going further in this direction. This hints at scenarios in which the impact of different forces is similar—in this case with the low capillary numbers this marks the beginning of a "capillary regime" in which capillary forces dominate. We complement the observation by investigating respective transport

networks that demonstrate comparable flow paths in Fig. 1. We also learn that higher capillary numbers yield a larger interfacial area, and in the following we further distinguish them into two characteristic cases (see Sec. 8 for a detailed discussion of our findings in porous media research).

Disconnected Components (Fig. 8b)

The number of disconnected components (i.e., blobs and ganglia) until breakthrough gives a complementary view on the behavior described by means of Fig. 8a. Most cases contain a limited number false positives (≤ 10) due to remaining artifacts after segmentation (see Sec. 3.2). The experiments ▪ (Ca 1e−2, M 1) and ▪ $(Ca = 1e−3, M = 0.2)$ stand out, indicating that the combination of high capillary number and low viscosity ratio creates many more isolated and disconnected blobs of the non-wetting phase than the other configurations. From this, we would expect the excluded experiment $(Ca = 1e−2, M = 0.2)$ to exhibit an even higher number of disconnected components, as high capillary number and low viscosity ratio favor such behavior. Additional experiments would be required to confirm this, as no reliable results could be obtained with our setup for this configuration (Sec. 3). It is also clearly reflected that as the viscosity ratio increases for high capillary numbers, the system changes from creating blobs to fluid progression in a narrow path (dubbed *fingers*)—as seen for ▪ $(Ca = 1e−2, M = 1)$ (g) and ▪ $(Ca = 1e−2, M = 10)$ (k) in Fig. 4. The formation of blobs is also one of two main causes identified in this work to be responsible for an increase in interfacial area (as seen in Fig. 8a).

Saturation of the Connected Wetting Phase (Fig. 8c)

The appearance of blobs and ganglia is one of the main reasons why we differentiate between connected and disconnected phases. Two groups of curves depicting the saturation of the connected wetting phase can clearly be identified in the diagram: one where the saturation settles between 0.3 and 0.5 (▪), and the rest (▪) where the saturation eventually approaches zero. Generally, breakthrough takes place at lower saturation for larger Ca. In addition, for increasing viscosity ratios, saturation after breakthrough steadily declines with eventually almost all wetting fluid being evicted (this is an important property for oil recovery, among other applications).

These findings indicate that for low capillary numbers, the flow is dominated by capillary forces, which induces the formation of so-called capillary fingers—thin, elongated flow structures, dictated exclusively by the local geometry of the pore space (the violet connected non-wetting phase in Fig. 6e shows an example). As the capillary number increases, a gradual switch can be observed from a capillary regime to a mixed capillary and viscous regime (where both viscous and capillary forces are significant). The further decrease in saturation indicates that viscous forces enable trapped wetting phase being freed after breakthrough (e.g., Fig. 6e in orange).

Blobs form when we increase the capillary number even further (for viscosity ratios $M \in \{0.2, 1\}$, Fig. 8b), caused by the competition between shear stresses and capillary forces. Fig. 8c shows that this further increases the saturation. The fluctuations in ▪ (Ca 1e−3, M 0.2) and ▪ (Ca 1e−2, M 1)) can be attributed to synergy effects with viscous fingering Fig. 4cg). As the viscosity ratio increases (M = 10), behavior changes to a piston-like movement of the non-wetting phase, with parallel fingers quickly invading a large part of the pore

space (▪ (Ca 1e−2, M 10) in Fig. 4k). Besides the formation of disconnected components, this constitutes the other identified main cause behind the increase in interfacial area seen in Fig. 8a (see Sec. 8 for further discussion).

7. Space-Time Analysis via Transport Networks

The analysis in Sec. 6 is based on scalar values—saturation, interfacial length, and disconnected components. While they quantitatively show how Ca and M affect the displacement process, they only implicitly indicate the resulting flow patterns. To directly capture and convey flow evolution with respect to the spatial domain, we propose a new visualization approach via so-called transport networks.

The general concept is based on pore network models which are widely used in porous media research for estimating material properties and simulation. Unfortunately, no precise definition of pores and throats exists, and prior approaches exhibit significant shortcomings [Blu01, XBJ16]. On the one hand, medial axis methods reduce the pore space to a topological skeleton, e.g., via thinning [BSM*96, LFMP98]. While this preserves the connectivity of the pore space, pores cannot be identified unambiguously anymore. On the other hand, the maximal ball algorithm finds the largest inscribed circles in the void space for each pixel and removes those included in other circles [AKB07, SP06]. The largest remaining circles identify pores, which are connected by the smaller remaining circles between them representing throats. However, the lack of a specific definition is a major problem with heterogeneous pore geometries like the one in this work. Neither medial axis nor maximum ball methods yield pore network models with a complete unambiguous mapping of void space to components.

These shortcomings are addressed with our (parameter-free) transport networks covering the complete void space. Nodes represent pores and edges reflect pore throats not only in terms of topology. By design, nodes and edges are associated with void space area such that there is no overlap and all of the void space is covered. This allows for a complete and unique mapping of fluid to pores and throats. A node-link representation then provides an aggregate overview of displacement progress for individual experiments before or after breakthrough (Sec. 7.1). Comparing them in a matrix layout enables linking flow evolution to the experiment parameter space (see Sec. 7.2 and Fig. 1). We further quantitatively link flow displacement to pore throats of different widths via transport networks and analyze the result with transport histograms (Sec. 7.3).

7.1. Transport Network Representation

We first create our transport network structure whose nodes (pores) and edges (throats) are associated with spatial coverage, yielding a partitioning of the complete void space. This allows to determine whether a pore, or throat, is occupied by the non-wetting fluid for each time step of an experiment based on the segmented phases. We finally discuss the visual mapping of transport networks to convey an aggregate overview on fluid progression patterns in the pore space.

Transport network structure. We propose to construct transport networks and their topology in a parameter-free way based on a triangulation of the void space, i.e., the part of the porous medium
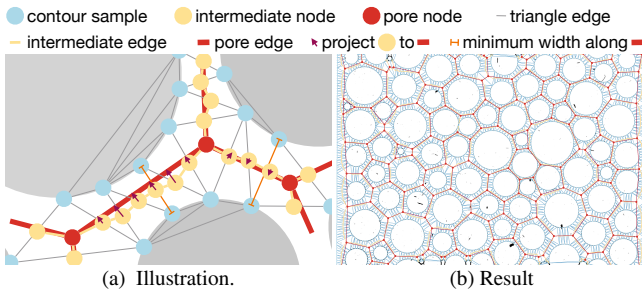
(a) Illustration.   (b) Result

Figure 9: For transport network generation, the contours of the solid are sampled (blue) and triangulated. Midpoints of edges not covered by solid become intermediate nodes (yellow). In the center of triangles with three intermediate nodes we insert a pore node (red), while triangles with two intermediate nodes induce intermediate edges (yellow lines). These intermediate edges are then aggregated to form connections between pore nodes (red lines).

that is available for fluid transport (Fig. 9). For this, we generate sample points at the solid interface (Sec. 5.1)—a step size of 20 pixels has proven to be sufficient to adequately resolve the domain (see blue points in Fig. 9a). Note that this was done with the purpose of reducing cost—in contrast to prior approaches whose parameters heavily influence the produced result (see discussion in Sec. 2). From these, we generate an unstructured triangular mesh via Delaunay triangulation.

Each triangle edge whose midpoint lies in void space becomes an intermediate node (yellow circle in Fig. 9a) and is added to our transport network. Next, we check the number of intermediate nodes for each triangle to distinguish whether it corresponds to a pore or a throat. In case there are two intermediate nodes, the triangle belongs to a throat. We add an intermediate edge connecting the intermediate nodes to our transport network (yellow line in Fig. 9a). If there are three intermediate nodes, the triangle belongs to a pore and a new pore node is inserted at the barycenter of the triangle (red circle in Fig. 9a). In addition, intermediate connections between the three intermediate nodes and the pore node are added as well.

The generated void space triangle mesh, nodes, and connections can be applied to all experiments that have been conducted with the same pore structure, after they have been aligned as described in Sec. 5. Crucially, this allows to directly compare experiments and analyze differences in flow processes.

Fluid occupancy. Each pore and throat segment are associated with one triangle covering a portion of the porous medium that is available for fluid flow. This allows us to register fluid occupancy with each component of the transport network by checking to what extent triangles cover areas filled with the non-wetting phase according to phase segmentation (Sec. 3.2).

For our analysis, we are interested in how long a pore, or a throat segment, is occupied by the non-wetting fluid in the considered time span, from the beginning of the process until breakthrough. We simply count a pore, or throat, as occupied at a given time step if the area of the associated triangle overlaps with non-wetting fluid (we use a minimum threshold of 10% to neglect small dust particles). Usage rate $\mathcal{U}$ then depicts the ratio with which the respective triangle is occupied by non-wetting phase over a given time span.

Visual representation. We visualize transport networks and corresponding fluid occupancy information with the goal of conveying a static overview on flow evolution before and after breakthrough. Our mapping is based on a node-link representation: nodes indicate pores (provided via pore nodes), whereas links denote throats, which are given as a sequence of intermediate line segments between two pore bodies. As we aim to compare flow evolution across different experiments via juxtaposition—we place experiments next to each other in a matrix layout reflecting the parameter space, see Sec. 7.2— it is crucial that also smaller representations are expressive.

For enhanced visual clarity in an overview visualization, we contract (purple arrows in Fig. 9a) the sequence of line segments depicting a throat to a straight pore edge connecting pore bodies (in red). We linearly map the minimum width of the respective pore throat to the thickness of the edge, as this metric is expected to have a strong influence on flow displacement. Triangle edge lengths provide a good approximation of pore width in our case (see Fig. 9b). The contracted edge consists of segments which correspond to one triangle each, and we map respective $\mathcal{U}$ to color via the Inferno color map [SvdWF15] (a perceptually uniform map depicting increasing $\mathcal{U}$ clearly with monotonically increasing luminance).

Another characteristic of interest for the analysis is the length of the considered interval in physical time. We encode this information in unoccupied pores and throats with $\mathcal{U} < 1\%$ (i.e, they would otherwise be mapped to black in our case). To be able to distinguish it clearly from $\mathcal{U}$ depicted with Inferno, we use a secondary isoluminant color map based on *CET-I1* by Kovesi [Kov15]. It consists of slightly saturated colors which do not divert the attention of the viewer and are also clearly distinct from Inferno.

The transport network to analyze how flow paths change after breakthrough is created in a slightly different way (Fig. 10). The usage rate is determined for the time interval before ($\mathcal{U}_{\text{before}}$) and after breakthrough ($\mathcal{U}_{\text{after}}$). $\mathcal{U}_{\text{after}}$ is mapped to color as described above, but segments with $\mathcal{U}_{\text{before}} > 1\%$ are mapped to black to indicate pore space already occupied before breakthrough.

7.2. Transport Network Matrix

To investigate the effects of Ca and M on flow behaviour, we create a small multiples visualization that arranges transport networks in a 2D matrix layout such that the position in the parameter space is reflected (akin to the glyphs introduced above). This allows to compare across all available combinations of Ca and M in a static visualization and to assess their impact on the spatio-temporal distribution of phases. In our analysis, we investigate two kinds of transport matrices, differing in the considered time span: before (Fig. 1) and after (Fig. 10) breakthrough. Their combination conveys a comprehensive qualitative and quantitative summary of flow progression. Among others, this yields new insights regarding the formation of large interfaces as well as the impact of forces after breakthrough. This will eventually lead us to the conclusion that Ca is ill-defined (see Sec. 8 for a discussion of findings in porous media research).

Before breakthrough (Fig. 1). First, we consider the time span from entry to breakthrough. Generally, the progression of the flow through the porous medium can be seen clearly, especially also
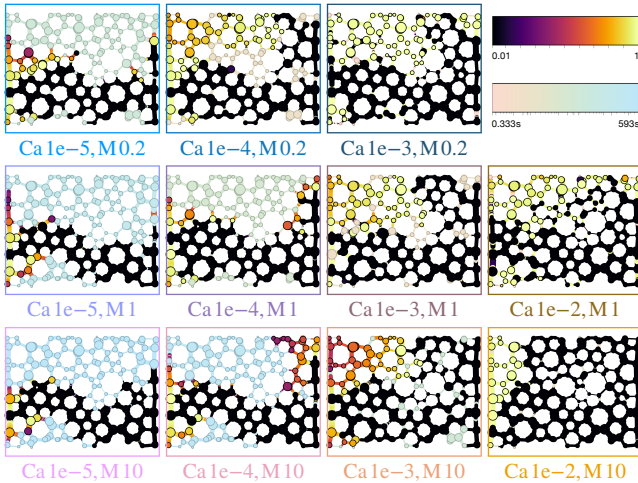
Figure 10: Transport networks of non-wetting flow after breakthrough (structures with fluid before breakthrough are depicted in black; color maps are akin to Fig. 1).
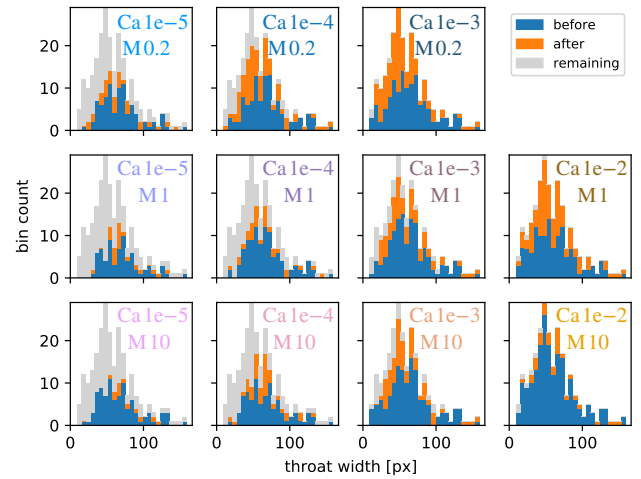

Figure 11: Histograms over minimum width of pore throats that transported the non-wetting phase before and after breakthrough; Fig. 1 (before) and Fig. 10 (after) for corresponding networks.

indicating for how long certain parts of the pore geometry were occupied via the depicted usage rate $\mathcal{U}$. Note that for this type of experiment, $\mathcal{U}$ directly corresponds to how soon a respective part is occupied, as the non-wetting phase retreats from a previously visited pore or throat only in few select cases.

Overall, different patterns can be observed that allow to draw conclusions regarding the impact of different forces in different areas of the parameter space. Experiments with low capillary number (■) yield comparably slow fluid progression in the form of a slim tongue, which is characteristic for a capillary regime. Viscosity ratio M only has little impact on the distribution of phases before breakthrough, yet we note that lower viscosity ratio results in a slightly broader path and processes running more quickly. Incremented Ca (■) yields qualitatively similar results, yet with a significantly increased influence of M. Further increasing the capillary number (■) interestingly yields new flow paths from the inlet in the upper part of the porous medium that evolve much later than the main flow below. This happens to some extent in all experiments, but is particularly significant in these cases. This effect requires further detailed investigation.

The combination of high capillary number Ca and viscosity ratio M (■) yields an almost uniform progression of the flow. Accordingly, the impact of the pore space is relatively small in the sense that the local pore geometry found in different parts of our solid does not seem to have a profound effect, since we no longer see fingers growing but a more-or-less stable front. This indicates a viscous regime (i.e., viscous forces dominate). In contrast, as indicated above, the flow paths with low capillary number and high viscosity ratio (■) clearly show the pore structure driving the flow along a certain path, which indicates a strong impact of capillary forces (i.e., hinting at a capillary regime). The cases in between exhibit an interesting interplay of both forces. A clear correspondence can be observed between experiment duration and flow patterns: fast experiments yield almost uniform "piston-like" progression, while slower experiments exhibit a narrow path. These observations are complemented with the analysis of quantities of interest which results in similar groups of outcomes despite considering other aspects (Sec. 6).

Generally, this shows that the phase occupancy at the boundary pores at the inlet and the outlet mostly depend on Ca, but there are also fluctuations between experiments in a viscous flow regime with large Ca. Resolving this issue by adapting the experimental setup is almost impossible in practice since for high capillary numbers even slight deviations can have a significant effect.

After breakthrough (Fig. 10). The extent of changes in pore space after breakthrough provides insights regarding the impact of different forces, and also supports partitioning of the parameter space into different regimes. For low capillary numbers Ca (■), we see that after breakthrough the usage rate does not change significantly since the capillary forces dominate the process, and the geometry of the porous medium is in charge of the process. The minor changes on the left can mostly be attributed to discontinuities at the outlet end (commonly denoted as *capillary end effects*). Intermediate capillary numbers with a medium or large viscosity ratio (■) yield similar results, yet with a stronger tendency toward newly visited pores close to the right boundary due to the increased impact of discontinuities at the inlet. For the same Ca, a low viscosity ratio M yields significant changes in the top-right, however. We also discover further progression with medium capillary numbers Ca and high viscosity ratio M (■), which we attribute to extensive viscous effects. As the capillary number is increased even further (■), we observe a further decrease in wetting phase saturation due to even stronger viscous forces. The characteristic that (almost) the whole pore space is occupied by non-wetting fluid for this configuration is an important property for numerous applications.

7.3. Pore Throat Histograms

Transport networks further allow us to analyze the relation between pore throat width and coverage with non-wetting fluid, which we show via histograms over the throat width using the same small multiples layout as above (Fig. 11). The histograms convey occupied pore throats before and after breakthrough, visualized as stacked bars in blue and orange, respectively. The remaining pore throats—which

never transport non-wetting fluid—are added on top as light-gray bars to convey the total distribution of pore throat widths as context.

These histograms in Fig. 11 complement the transport network visualization in Fig. 1 and Fig. 10, covering both time periods (before/after breakthrough) in one view and enabling a quantitative comparison of throat occupation. Different aspects already discovered in the transport network visualizations can be investigated in more detail. Generally, larger Ca lead to a higher saturation, with Ca $\in \{1e-3, 1e-2\}$ yielding (almost) full saturation of the porous medium eventually (▮). This also quantitatively underlines the observation that high Ca in combination with low M leads to viscous fingering (▮), low Ca with practically any M yields capillary fingering (▮), and high Ca together with high M results in a stable front that yields (almost) full saturation eventually after breakthrough (▮). The experiments in-between in the parameter space exhibit a mixture of these characteristics (▮). It is also confirmed that—across all experiments—a lower coverage is achieved for smaller throat widths. This is due to an increase of so-called capillary pressure—resulting from the interaction of interfacial tension between the fluids and the affinity of the wetting phase to the solid—which in this case opposes fluid transport and increases with smaller Ca.

8. Discussion and Future Work

This paper both discusses our visualization approach for the visual analysis of two-phase fluid flow in a porous medium and presents the new insights from an experimental parameter study.

Visual representations. Our visual analysis approach enabled our domain experts to effectively study characteristic flow patterns influenced by pore geometry as well as the combination of viscous and capillary forces. It proved beneficial to build upon well-known visualization concepts like line charts and histograms, whenever possible. Our new node-link transport network representation has further shown to be effective due to its natural geometrical embedding in the physical setup. Major design considerations across all visualizations included the comparison between experiments and their positions in the parameter space.

In each of the charts showing characteristic quantities, every experiment can be depicted by one line each in a straightforward fashion. We first solely relied on a bivariate color map for associating lines with the parameter space, which, however, proved to be difficult to interpret. The introduction of parameter space glyphs as annotations to the charts significantly improved the mapping of lines to the parameter space, and further greatly facilitated the discussion of respective results by using them as graphical representatives.

For the number of experiments in our ensemble, juxtaposition in a matrix layout is an effective means for the comparison across transport networks and histograms. There might be difficulties regarding visual scalability for an extended ensemble though. For the transport network matrices presented in this work, we already found it helpful to improve visual clarity by contracting pore edges.

The visualizations were iteratively refined in close discussion between visualization researchers and domain experts. In particular, it was found to be challenging to compare findings regarding the parameter space across our different types of visualizations and to

map specific parameter values to the parameter space layout. The implementation of a consistent parameter space layout across matrices of transport networks and histograms as well as the glyphs annotating the charts has shown to be highly beneficial in this regard. Still, directly linking individual representations—e.g, within a visual analysis system—would have facilitated what has proven to be an important part of the analysis.

Findings in porous media research. Identifying and classifying experiments with similar behavior allows us to partition the experiment parameter space into regimes and relate them to the dominant driving forces (i.e., capillary forces, viscous forces, and combinations thereof). Through visual analysis, we newly identified two characteristic cases leading to large interfaces: competing viscous and capillary forces inducing breakup of the non-wetting phase, and the creation of thin fingers. We further investigate the validity of Lenormand's theory regarding the partitioning into different flow regimes based on Ca and M [LTZ88]. Ca $= 1e-5$ (▮) should correspond to a capillary-dominated flow regime, and also yield similar flow displacement characteristics for a capillary regime across viscosity ratios M (see Fig. 1). However, after breakthrough, something unexpected happens for a capillary regime (Fig. 10): there is further expansion of the occupancy of the non-wetting phase, inversely proportional to M. This is surprising since there is an established low resistance path for the non-wetting phase. This needs to be attributed to the impact of viscous forces, which is underlined by the identified impact of M. From our results, we claim that only ▮(Ca $1e-5$,M 10) is an (almost) exclusively capillarity-dominated case, with other experiments exhibiting viscous contribution of varying degree as indicated by post-breakthrough changes. Note that Ca and M are interconnected for a given pair of fluids, and when changing M an inverse change in flow velocity is required to keep Ca constant (i.e, the flow velocity must be 50× higher for M $= 0.2$ in comparison to M $= 10$ to yield the same Ca). The 50× slower flow velocity for M $= 10$ also means accordingly slower breakthrough, providing the overall system more time to reach a steady state. The system becomes more dynamic and unstable for larger Ca, and gradually switches from a capillarity-dominated regime to a purely viscous one. With our visual analysis approach, we are now able to demonstrate that Ca is ill-defined. While it considers velocity at the inlet, the heterogeneous pore geometry yields variations in local velocity— and with this Ca—across the porous medium. This means that the local Ca yielding breakthrough can not clearly be attributed solely to capillary forces anymore. Depending on the spatial configuration of the porous medium in the vicinity of breakthrough, this may trigger a sequence of events leading to a deviation from a purely capillary regime (we observe this in Fig. 10 and Fig. 11).

Future work in porous media research. These findings demonstrate the need for additional metrics characterizing the flow regime in a porous medium. It is apparent now that information related to the capillary number and the viscosity ratio is not enough, and information regarding the geometrical distribution of the pore space is probably the missing link. In general, our experiments exhibit physical effects that are challenging to model due to the increased physical complexity of the processes involved. While micro-scale approaches exist, they cannot adequately model all observed effects, whereas macro-scale models do not consider some effects at all (e.g., the reduction of effective interfacial area between solid and non-

wetting fluid is not appropriately reflected). Based on the extracted data and findings of this work, we can, for the first time, attempt to effectively model the respective processes. We aim to investigate the role of the solid phase geometry more closely as well as its interplay with Ca and M. For this, we plan to repeat the experiments with pore structures exhibiting similar average properties (like porosity), but different geometries (locally and globally). We also intend to extend our research to scenarios other than primary drainage, and evaluate the role of the pore bodies and throats as the dominant geometrical measure of each displacement process. This is directly linked to the so-called Young-Laplace equation describing the capillary pressure difference between two fluids which is also dominantly affected by the local geometrical properties of the porous medium. Pore bodies are the determining feature for drainage, due to their increased size and lower entry capillary pressure for an invasion process, while pore throats are dominant during imbibition due to their reduced size and the spontaneous response of the system to the increased capillarity. Finally, we aim to investigate the conditions under which fluid components can become disconnected, and how they interact with and influence flow evolution.

Future work in visualization. The planned efforts in porous media research will require additional experiments, yielding an extended and more densely sampled parameter space. This poses significant additional challenges for the visual analysis. In particular, different directions for enhanced visual scalability of our visualization approaches will be investigated. First of all, while our matrix layout of transport networks proved to be crucial in our analysis, it does not directly scale visually to larger experiment and/or simulation ensembles. However, transport networks provide an abstract representation of the pore geometry that could further be scaled towards more expressive smaller representations (like glyphs) by reducing the underlying graph accordingly. We already take a small step in this direction in this work with the contraction of throat segments to a straight line for visual clarity, but more advanced measures are needed for the analysis of much larger ensembles. We further aim to supplement the analysis with additional quantities that could prove to be relevant (e.g., distinguishing disconnected components into ganglia and blobs and quantifying shape via descriptors). This accordingly results in a high-dimensional feature vector describing each experiment that could be the basis for further analysis techniques based on projection and/or clustering.

Furthermore, in this work, we employ the same porous medium for the sake of direct comparability. An extended study, however, will include different models for a more targeted investigation of specific effects as outlined above. However, direct spatial comparison across different pore geometries will not be possible anymore, but needs to be substituted by more abstract alternatives. In particular, this means relying more strongly on extracted quantities that still incorporate pore-space properties, like transport histograms in this work. Perspectively, 3D experiments (and simulations) could also be conducted for further investigation. Quantity extraction generally works akin to 2D, and transport networks can be generalized to 3D by discretizing the porous medium with tetrahedra instead of triangles. However, we anticipate that the direct 3D visualization of a complex transport network will exhibit issues regarding clutter and visual clarity. This could be addressed with a combination of condensing the visual representation and focus+context-style exploration, po-

tentially linked with views showing extracted quantities for a more comprehensive visual analysis approach for porous media research.

Acknowledgments

References

[ABB13] ANDREW M., BIJELJIC B., BLUNT M. J.: Pore-scale imaging of geological carbon dioxide storage under in situ conditions. *Geophysical Research Letters 40*, 15 (2013), 3915–3918. URL: https://agupubs.onlinelibrary.wiley.com/doi/abs/10.1002/grl.50771, arXiv:https://agupubs.onlinelibrary.wiley.com/doi/pdf/10.1002/grl.50771, doi:10.1002/grl.50771. 3

[AKB07] AL-KHARUSI A. S., BLUNT M. J.: Network extraction from sandstone and carbonate pore space images. *Journal of Petroleum Science and Engineering 56*, 4 (Apr. 2007), 219–231. URL: https://www.sciencedirect.com/science/article/pii/S092041050600204X, doi:10.1016/j.petrol.2006.09.003. 7

[AMW*17] ALZAHID Y., MOSTAGHIMI P., WARKIANI M. E., ARMSTRONG R. T., JOEKAR-NIASAR V., KARADIMITRIOU N., ET AL.: Alkaline surfactant polymer flooding: what happens at the pore scale? In *SPE Europec featured at 79th EAGE Conference and Exhibition* (2017), Society of Petroleum Engineers. 2

[Blu01] BLUNT M. J.: Flow in porous media—pore-network models and multiphase flow. *Current opinion in colloid & interface science 6*, 3 (2001), 197–207. 7

[BM10] BRUCKNER S., MOLLER T.: Result-Driven Exploration of Simulation Parameter Spaces for Visual Effects Design. *IEEE Transactions on Visualization and Computer Graphics 16*, 6 (Nov. 2010), 1468–1476. doi:10.1109/TVCG.2010.190. 3

[BOK*13] BERG S., OTT H., KLAPP S. A., SCHWING A., NEITELER R., BRUSSEE N., MAKURAT A., LEU L., ENZMANN F., SCHWARZ J.-O., KERSTEN M., IRVINE S., STAMPANONI M.: Real-time 3d imaging of haines jumps in porous media flow. *Proceedings of the National Academy of Sciences 110*, 10 (2013), 3755–3759. URL: https://www.pnas.org/content/110/10/3755, arXiv:https://www.pnas.org/content/110/10/3755.full.pdf, doi:10.1073/pnas.1221373110. 3

[BRB*16] BARTELS W., RÜCKER M., BERG S., MAHANI H., GEORGIADIS A., BRUSSEE N., COORN A., VAN DER LINDE H., FADILI A., HINZ C., ET AL.: Micro-ct study of the impact of low salinity waterflooding on the pore-scale fluid distribution during flow. In *International Symposium of the Society of Core Analysts, Snowmass, CO* (2016), vol. 22, pp. 1362–1373. 3

[BSM*96] BALDWIN C. A., SEDERMAN A. J., MANTLE M. D., ALEXANDER P., GLADDEN L. F.: Determination and Characterization of the Structure of a Pore Space from 3D Volume Images. *Journal of Colloid and Interface Science 181*, 1 (July 1996), 79–92. URL: https://www.sciencedirect.com/science/article/pii/S0021979796903586, doi:10.1006/jcis.1996.0358. 7

[CCR97] CORAPCIOGLU Y. M., CHOWDHURY S., ROOSEVELT S. E.: Micromodel visualization and quantification of solute transport in porous media. *Water Resources Research 33*, 11 (1997), 2547–2558. URL: https://agupubs.onlinelibrary.wiley.com/doi/abs/10.1029/97WR02115, arXiv:https://agupubs.onlinelibrary.wiley.com/doi/pdf/10.1029/97WR02115, doi:10.1029/97WR02115. 3

[CPNNG04] CHENG J.-T., PYRAK-NOLTE L. J., NOLTE D. D., GIORDANO N. J.: Linking pressure and saturation through interfacial areas in porous media. *Geophysical Research Letters 31*, 8 (2004). URL: https://agupubs.onlinelibrary.wiley.com/doi/abs/10.1029/2003GL019282, arXiv:https://agupubs.onlinelibrary.wiley.com/doi/pdf/10.1029/2003GL019282, doi:10.1029/2003GL019282. 3

[Dar57] DARCY H.: *Recherches expérimentales relatives au mouvement de l'eau dans les tuyaux.* No. v. 1 in Recherches expérimentales relatives au mouvement de l'eau dans les tuyaux. Impr. Impériale, 1857. URL: https://books.google.de/books?id=s88WAAAAQAAJ. 3

[dWWS*20] DE WINTER D. A. M., WEISHAUPT K., SCHELLER S., FREY S., RAOOF, A. H., S. M. HELMIG R.: The complexity of porous media flow characterized in a microfluidic model based on confocal laser scanning microscopy and micro-piv. *Transport in Porous Media* (2020), 1573–1634. doi:10.1007/s11242-020-01515-9. 3

[EP08] EVANGELIDIS G. D., PSARAKIS E. Z.: Parametric image alignment using enhanced correlation coefficient maximization. *IEEE Transactions on Pattern Analysis and Machine Intelligence 30*, 10 (2008), 1858–1865. 4

[FGT16] FAVELIER G., GUEUNET C., TIERNY J.: Visualizing ensembles of viscous fingers. 3

[FHR04] FAISAL I. K., HUSAIN T., RAMZI H.: An overview and analysis of site remediation technologies. *Journal of Environmental Management 71*, 2 (2004), 95 – 122. URL: http://www.sciencedirect.com/science/article/pii/S0301479704000313, doi:https://doi.org/10.1016/j.jenvman.2004.02.003. 2

[GCS88] GROSSER K., CARBONELL R., SUNDARESAN S.: Onset of pulsing in two-phase cocurrent downflow through a packed bed. *AIChE Journal 34*, 11 (1988), 1850–1860. 3

[GG16] GEVECI B., GARTH C.: Scientific Visualization Contest 2016, 2016. URL: https://www.uni-kl.de/sciviscontest. 3

[GGS*18] GRALKA P., GROTTEL S., STAIB J., SCHATZ K., KARCH G. K., HIRSCHLER M., KRONE M., REINA G., GUMHOLD S., ERTL T.: 2016 ieee scientific visualization contest winner: Visual and structural analysis of point-based simulation ensembles. *IEEE Computer Graphics and Applications 38*, 3 (2018), 106–117. doi:10.1109/MCG.2017.3301120. 3

[GRZ*10] GROTTEL S., REINA G., ZAUNER T., HILFER R., ERTL T.: Particle-based Rendering for Porous Media. In *Proceedings of the annual SIGRAD conference* (2010), Jää-Aro K.-M., Larsson T., (Eds.), vol. 52, Linköping University Electronic Press, pp. 45–51. Publication Title: SIGRAD. 3

[HG93] HASSANIZADEH S. M., GRAY W. G.: Thermodynamic basis of capillary pressure in porous media. *Water resources research 29*, 10 (1993), 3389–3405. 3

[HGSP20] HE W., GUO H., SHEN H.-W., PETERKA T.: eFESTA: Ensemble Feature Exploration with Surface Density Estimates. *IEEE Transactions on Visualization and Computer Graphics 26*, 4 (Apr. 2020), 1716–1731. doi:10.1109/TVCG.2018.2879866. 3

[HHB16] HAO L., HEALEY C. G., BASS S. A.: Effective Visualization of Temporal Ensembles. *IEEE Transactions on Visualization and Computer Graphics 22*, 1 (Jan. 2016), 787–796. doi:10.1109/TVCG.2015.2468093. 3

[HOGJ13] HUMMEL M., OBERMAIER H., GARTH C., JOY K. I.: Comparative Visual Analysis of Lagrangian Transport in CFD Ensembles. *IEEE Transactions on Visualization and Computer Graphics 19*, 12 (Dec. 2013), 2743–2752. doi:10.1109/TVCG.2013.141. 3

[HSZ87] HARALICK R. M., STERNBERG S. R., ZHUANG X.: Image Analysis Using Mathematical Morphology. *IEEE Transactions on Pattern Analysis and Machine Intelligence PAMI-9*, 4 (July 1987), 532–550. Conference Name: IEEE Transactions on Pattern Analysis and Machine Intelligence. doi:10.1109/TPAMI.1987.4767941. 4

[KH12] KARADIMITRIOU N. K., HASSANIZADEH S. M.: A review of micromodels and their use in two-phase flow studies. *Vadose Zone Journal 11*, 3 (2012), vzj2011.0072. URL: https://acsess.onlinelibrary.wiley.com/doi/abs/10.2136/vzj2011.0072, arXiv:https://acsess.onlinelibrary.wiley.com/doi/pdf/10.2136/vzj2011.0072, doi:10.2136/vzj2011.0072. 3

[KH13] KEHRER J., HAUSER H.: Visualization and visual analysis of multifaceted scientific data: A survey. *IEEE transactions on visualization and computer graphics 19*, 3 (Mar. 2013), 495–513. doi:10.1109/TVCG.2012.110. 3

[KHJNK14] KARADIMITRIOU N. K., HASSANIZADEH S. M., JOEKAR-NIASAR V., KLEINGELD P. J.: Micromodel study of two-phase flow under transient conditions: Quantifying effects of specific interfacial area. *Water Resources Research 50*, 10 (2014), 8125–8140. URL: https://agupubs.onlinelibrary.wiley.com/doi/abs/10.1002/2014WR015388, arXiv:https://agupubs.onlinelibrary.wiley.com/doi/pdf/10.1002/2014WR015388, doi:10.1002/2014WR015388. 3

[KLG10] KETTLE J., LAMMINMÄKI T., GANE P.: A review of modified surfaces for high speed inkjet coating. *Surface and Coatings Technology 204*, 12 (2010), 2103 – 2109. Proceedings of the European Materials Research Socierty (E-MRS)Spring Meeting 2009. URL: http://www.sciencedirect.com/science/article/pii/S0257897209008433, doi:https://doi.org/10.1016/j.surfcoat.2009.10.035. 2

[KMK*13] KARADIMITRIOU N. K., MUSTERD M., KLEINGELD P. J., KREUTZER M. T., HASSANIZADEH S. M., JOEKAR-NIASAR V.: On the fabrication of pdms micromodels by rapid prototyping, and their use in two-phase flow studies. *Water Resources Research 49*, 4 (2013), 2056–2067. URL: https://agupubs.onlinelibrary.wiley.com/doi/abs/10.1002/wrcr.20196, arXiv:https://agupubs.onlinelibrary.wiley.com/doi/pdf/10.1002/wrcr.20196, doi:10.1002/wrcr.20196. 3

[Kov15] KOVESI P.: Good colour maps: How to design them. *arXiv preprint arXiv:1509.03700* (2015). 8

[KRRW19] KUMPF A., RAUTENHAUS M., RIEMER M., WESTERMANN R.: Visual Analysis of the Temporal Evolution of Ensemble Forecast Sensitivities. *IEEE Transactions on Visualization and Computer Graphics 25*, 1 (Jan. 2019), 98–108. doi:10.1109/TVCG.2018.2864901. 3

[KS14] KURZEJA P. S., STEEB H.: Variational formulation of oscillating fluid clusters and oscillator-like classification. ii. numerical study of pinned liquid clusters. *Physics of Fluids 26*, 4 (2014), 042107. 3

[LAS*17] LUKASCZYK J., ALDRICH G., STEPTOE M., FAVELIER G., GUEUNET C., TIERNY J., MACIEJEWSKI R., HAMANN B., LEITTE H.: Viscous fingering: A topological visual analytic approach. In *Applied Mechanics and Materials* (2017), vol. 869, Trans Tech Publ, pp. 9–19. 3

[LBS*18] LUCIANI T., BURKS A., SUGIYAMA C., KOMPERDA J., MARAI G. E.: Details-first, show context, overview last: Supporting exploration of viscous fingers in large-scale ensemble simulations. *IEEE transactions on visualization and computer graphics 25*, 1 (2018), 1–11. 3

[LFMP98] LIANG Z. R., FERNANDES C. P., MAGNANI F. S., PHILIPPI P. C.: A reconstruction technique for three-dimensional porous media using image analysis and Fourier transforms. *Journal of Petroleum Science and Engineering 21*, 3 (Nov. 1998), 273–283. URL: https://www.sciencedirect.com/science/article/pii/S0920410598000771, doi:10.1016/S0920-4105(98)00077-1. 7

[LTZ88] LENORMAND R., TOUBOUL E., ZARCONE C.: Numerical models and experiments on immiscible displacements in porous media. *Journal of fluid mechanics 189* (1988), 165–187. 3, 10

[MK61] MATTAX C., KYTE J.: Ever see a water flood. *Oil Gas J 59*, 42 (1961), 115–128. 3

[NBK13] NAUMOV D., BILKE L., KOLDITZ O.: Rendering Technique of Multi-layered Domain Boundaries and its Application to

Fluid Flow in Porous Media Visualizations. *Workshop on Visualisation in Environmental Sciences (EnvirVis)* (2013), 4 pages. Artwork Size: 4 pages ISBN: 9783905674545 Publisher: The Eurographics Association. URL: http://diglib.eg.org/handle/10.2312/PE.EnvirVis.EnvirVis13.043-046, doi:10.2312/PE.ENVIRVIS.ENVIRVIS13.043-046. 3

[OJ14] OBERMAIER H., JOY K. I.: Future challenges for ensemble visualization. *IEEE Computer Graphics and Applications 34*, 3 (May 2014), 8–11. doi:10.1109/MCG.2014.52. 3

[PWB*09] POTTER K., WILSON A., BREMER P.-T., WILLIAMS D., DOUTRIAUX C., PASCUCCI V., JOHNSON C. R.: Ensemble-Vis: A Framework for the Statistical Visualization of Ensemble Data. In *In Proceedings of the 2009 IEEE International Conference on Data Mining Workshops* (2009), pp. 233–240. doi:10.1109/ICDMW.2009.55. 3

[S*85] SUZUKI S., ET AL.: Topological structural analysis of digitized binary images by border following. *Computer vision, graphics, and image processing 30*, 1 (1985), 32–46. 4

[SBR*16] SCHLÜTER S., BERG S., RÜCKER M., ARMSTRONG R., VOGEL H.-J., HILFER R., WILDENSCHILD D.: Pore-scale displacement mechanisms as a source of hysteresis for two-phase flow in porous media. *Water Resources Research 52*, 3 (2016), 2194–2205. 3

[Sha98] SHAW H.: *Investigation of the Nature of Surface Resistance of Water and of Stream-line Motion Under Certain Experimental Conditions*. Inst. N.A., 1898. URL: https://books.google.de/books?id=PIcdHAAACAAJ. 3

[SHB*14] SEDLMAIR M., HEINZL C., BRUCKNER S., PIRINGER H., MÖLLER T.: Visual Parameter Space Analysis: A Conceptual Framework. *IEEE Transactions on Visualization and Computer Graphics 20*, 12 (Dec. 2014), 2161–2170. doi:10.1109/TVCG.2014.2346321. 3

[SP06] SILIN D., PATZEK T.: Pore space morphology analysis using maximal inscribed spheres. *Physica A: Statistical Mechanics and its Applications 371*, 2 (Nov. 2006), 336–360. URL: https://www.sciencedirect.com/science/article/pii/S037843710600464X, doi:10.1016/j.physa.2006.04.048. 7

[SPD*19] SOLER M., PETITFRERE M., DARCHE G., PLAINCHAULT M., CONCHE B., TIERNY J.: Ranking viscous finger simulations to an acquired ground truth with topology-aware matchings. In *2019 IEEE 9th Symposium on Large Data Analysis and Visualization (LDAV)* (2019), IEEE, pp. 62–72. 3

[SS18] SIVANESAPILLAI R., STEEB H.: Fluid interfaces during viscous-dominated primary drainage in 2d micromodels using pore-scale sph simulations. *Geofluids 2018* (2018). 3

[SvdWF15] SMITH N. J., VAN DER WALT S., FIRING E.: colormaps.py. https://github.com/BIDS/colormap, 2015. 8

[SZD*10] SANYAL J., ZHANG S., DYER J., MERCER A., AMBURN P., MOORHEAD R.: Noodles: A Tool for Visualization of Numerical Weather Model Ensemble Uncertainty. *IEEE Transactions on Visualization and Computer Graphics 16*, 6 (Nov. 2010), 1421–1430. doi:10.1109/TVCG.2010.181. 3

[Tho83] THOMPSON L. F.: *An Introduction to Lithography*. American Chemical Society, 1983, ch. 1, pp. 1–13. doi:10.1021/bk-1983-0219.ch001. 3

[VG80] VAN GENUCHTEN M. T.: A closed-form equation for predicting the hydraulic conductivity of unsaturated soils 1. *Soil science society of America journal 44*, 5 (1980), 892–898. 3

[WCBP12] WIDANAGAMAACHCHI W., CHRISTENSEN C., BREMER P.-T., PASCUCCI V.: Interactive exploration of large-scale time-varying data using dynamic tracking graphs. In *IEEE Symposium on Large Data Analysis and Visualization (LDAV)* (2012), pp. 9–17. doi:10.1109/LDAV.2012.6378962. 3

[Web01] WEBSTER R.: Statistical analysis of microstructures in materials science. *European Journal of Soil Science 52*, 3 (2001), 527–527. 3

[WFR*10] WASER J., FUCHS R., RIBICIC H., SCHINDLER B., BLOSCHL G., GROLLER E.: World Lines. *IEEE Transactions on Visualization and Computer Graphics 16*, 6 (Nov. 2010), 1458–1467. doi:10.1109/TVCG.2010.223. 3

[WHLS19] WANG J., HAZARIKA S., LI C., SHEN H.: Visualization and Visual Analysis of Ensemble Data: A Survey. *IEEE Transactions on Visualization and Computer Graphics 25*, 9 (Sept. 2019), 2853–2872. doi:10.1109/TVCG.2018.2853721. 3

[XBJ16] XIONG Q., BAYCHEV T. G., JIVKOV A. P.: Review of pore network modelling of porous media: experimental characterisations, network constructions and applications to reactive transport. *Journal of contaminant hydrology 192* (2016), 101–117. 7

[XDH*19] XU J., DUTTA S., HE W., MOORTGAT J., SHEN H.-W.: Geometry-driven detection, tracking and visual analysis of viscous and gravitational fingers. *arXiv preprint arXiv:1911.12383* (2019). 3

[XW98] XIA Y., WHITESIDES G. M.: Soft lithography. *Angewandte Chemie International Edition 37*, 5 (1998), 550–575. doi:10.1002/(SICI)1521-3773(19980316)37:5<550::AID-ANIE550>3.0.CO;2-G. 3

[ZFS*18] ZHANG H., FREY S., STEEB H., URIBE D., ERTL T., WANG W.: Visualization of bubble formation in porous media. *IEEE transactions on visualization and computer graphics 25*, 1 (2018), 1060–1069. 3